1   **Single-cell selectivity and functional architecture of human lateral occipital complex**

2   Functional architecture of LOC

3

4   Thomas Decramer[1,2,3]#, Elsie Premereur[1]#*, Mats Uytterhoeven[3], Wim Van Paesschen[4,5], Johannes

5   van Loon[2,3], Peter Janssen[1]+, Tom Theys[2,3]+

6   1. Laboratory for Neuro- and Psychophysiology, KU Leuven and the Leuven Brain Institute,

7   Leuven, Belgium

8   2. Department of Neurosurgery, University Hospitals Leuven, Leuven, Belgium

9   3. Research Group Experimental Neurosurgery and Neuroanatomy, KU Leuven and the Leuven

10   Brain Institute, Leuven, Belgium

11   4. Department of Neurology, University Hospitals Leuven, Leuven, Belgium

12   5. Laboratory for Epilepsy Research, KU Leuven, Leuven, Belgium

13

14   #shared first author; +shared senior author

15   *Lead Contact: elsie.premereur@kuleuven.be

16   **Author contributions**

17   TD, EP, PJ and TT designed experiment

18   TD, MU and TT collected data

19   EP, TD performed data-analysis

20   TD, EP, PJ, TT, WVP, and JvL wrote the paper

Abstract

The human lateral occipital complex (LOC) is more strongly activated by images of objects compared to scrambled controls, but detailed information at the neuronal level is currently lacking. We recorded with microelectrode arrays in the LOC of two patients, and obtained highly selective single-unit, multi-unit and high-gamma responses to images of objects. Contrary to predictions derived from functional imaging studies, all neuronal properties indicated that the subsector of LOC we recorded from occupies an unexpectedly high position in the hierarchy of visual areas. Notably, the response latencies of LOC neurons were long, the shape selectivity was spatially clustered, LOC receptive fields were large and bilateral, and a number of LOC neurons exhibited 3D-structure selectivity (a preference for convex or concave stimuli), which are all properties typical of end-stage ventral stream areas. Thus, our results challenge prevailing ideas about the position of the LOC in the hierarchy of visual areas.

Introduction

Our understanding of the human brain is hampered by the limitations imposed upon neuroscience research in humans. Noninvasive measurements of brain activity (EEG, functional Magnetic Resonance Imaging or fMRI) often provide only coarse information regarding neural activity, due to their limited spatial or temporal resolution. Genuine insight into the function of a brain area requires detailed measurements of the electrical activity of individual neurons and small populations of neurons at high spatiotemporal resolution. Intracortical electrophysiological recordings in humans are scarce, therefore the human visual cortex is virtually unexplored at the level of the individual neurons and small populations of neurons. Several studies have recorded field potentials with intracranial electrodes (Allison et al., 1999, Arroyo et al., 1993, Yoshor et al., 2007), but macroelectrode recordings still reflect activity of hundreds of thousands of neurons and, due to their large contact area, cannot measure spiking activity, nor can they reveal the microarchitecture of visual

45   cortex on a submillimeter scale. A series of studies using depth electrodes in the mesial temporal lobe

46   have investigated the visual responses of single neurons in entorhinal and perirhinal cortex (Fried et

47   al., 1997, Kreiman et al., 2000b, Kreiman et al., 2000a, Kreiman et al., 2002, Quiroga et al., 2005, Quian

48   Quiroga et al., 2009), and one study (Aflalo et al., 2015) reported single-unit responses during

49   imagined actions (reaching and grasping) in a patient with a microelectrode array implanted in parietal

50   cortex, who thereby obtained accurate control over a robot arm. (Self et al., 2016) measured multi-

51   unit activity (MUA) and local field potential (LFP) activity in early visual areas (V2/V3) in a patient using

52   hybrid macro-micro depth electrodes. This study observed that the properties of populations of

53   neurons (multi-unit receptive fields, tuning for contrast, orientation, spatial frequency and modulation

54   by context and attention) were similar to those of neurons in the macaque areas V2 and V3. To our

55   knowledge, intracortical recordings in intermediate human visual areas such as the Lateral Occipital

56   Complex (LOC) have never been performed.

57   Recordings in patients, combined with similar measurements in monkeys, may allow us to

58   answer very specific questions with regard to the properties of individual neurons and the homologies

59   between cortical areas in humans and monkeys. For example, assessing the shape selectivity or the

60   receptive field profile of LOC neurons requires intracortical recordings, which have never been

61   performed. Moreover, despite two decades of functional imaging studies in both species (Vanduffel

62   et al., 2014), the homologies between the (subsectors of) LOC and ventral occipitotemporal cortex in

63   humans and the monkey inferior temporal cortex (ITC) areas has not yet been resolved. The LO1 and

64   LO2 subsector may be retinotopically organized (Wandell et al., 2007, Silson et al., 2013), similar to

65   the monkey area TEO (Boussaoud et al., 1991), but direct single-cell evidence in the two species is

66   lacking. Furthermore, the microarchitecture of these areas in humans (i.e. the spatial clustering of

67   shape selectivity on the scale of cortical columns measuring 0.5 mm) is very difficult to assess with

68   fMRI (Goncalves et al., 2015). To investigate the clustering of neuronal selectivity in human visual

69   cortex, recordings with intracortical microelectrodes are necessary.

70

71   **Results**

72   In two patients who were evaluated for refractory epilepsy, we ran an LOC-localizer fMRI

73   experiment, in which blocks of non-scrambled shapes and outlines were interleaved with control

74   blocks of scrambled stimuli (Fig. 1, (Kourtzi and Kanwisher, 2000)). A 96-channel Utah microelectrode

75   array was implanted in LOC (Fig. 1A; MNI coordinates 55, -71, 1 for patient 1, and -55, -77, 6 for patient

76   2) (Silson et al., 2013). We verified the anatomical location of the array using a computed tomography

77   (CT) scan obtained after array implantation, which was co-registered onto the anatomical MRI. Figure

78   1B shows the fMRI activations in the two patients for the contrast non-scrambled vs. scrambled

79   stimuli, plotted on the patient's own anatomical MRI (p<0.05, FWE corrected). The fMRI results

80   confirmed that the microelectrode arrays were indeed implanted in the hotspot of fMRI activations.
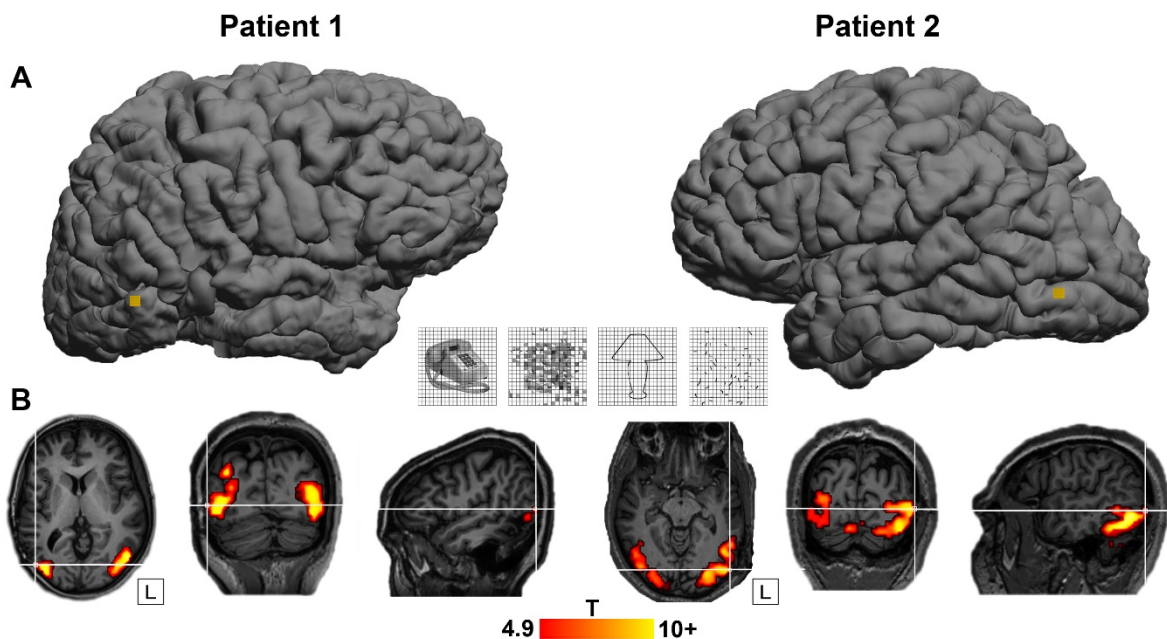

81

82   *Figure 1. LO Localizer and location of arrays. A. Site of Utah array implantation (yellow)*
83   *projected onto 3D rendering of the brain in patient 1 (left) and patient 2 (right). Center: LO Localizer*
84   *stimuli (shapes, scrambled shapes, outlines, scrambled outlines). B. fMRI activations with LO localizer*
85   *stimuli. T-values for contrast [shapes+outlines]-[scrambled shapes+scrambled outlines], plotted on T1*
86   *weighted image. P<0.05, FWE-corrected for multiple comparisons. Crosshair indicates the position of*
87   *the Utah array in relation to the fMRI activation for both patients.*

88

4

89   **Effect of image scrambling**

90   The example neuron in Figure 2A responded significantly more strongly to images of objects

91   (both shapes and outlines) compared to scrambled controls (permutation test: p <0.001, d' = 0.72 for

92   shapes and p = 0.002, d' = 0.50 for line stimuli). Unlike previous recordings in the human medial

93   temporal lobe (Kreiman et al., 2000b, Quiroga et al., 2005), this neuronal response was brisk and

94   relatively transient (response and selectivity latency: 125 ms). The large waveform (inset in Figure 2A)

95   indicates that this neuron was well-isolated.
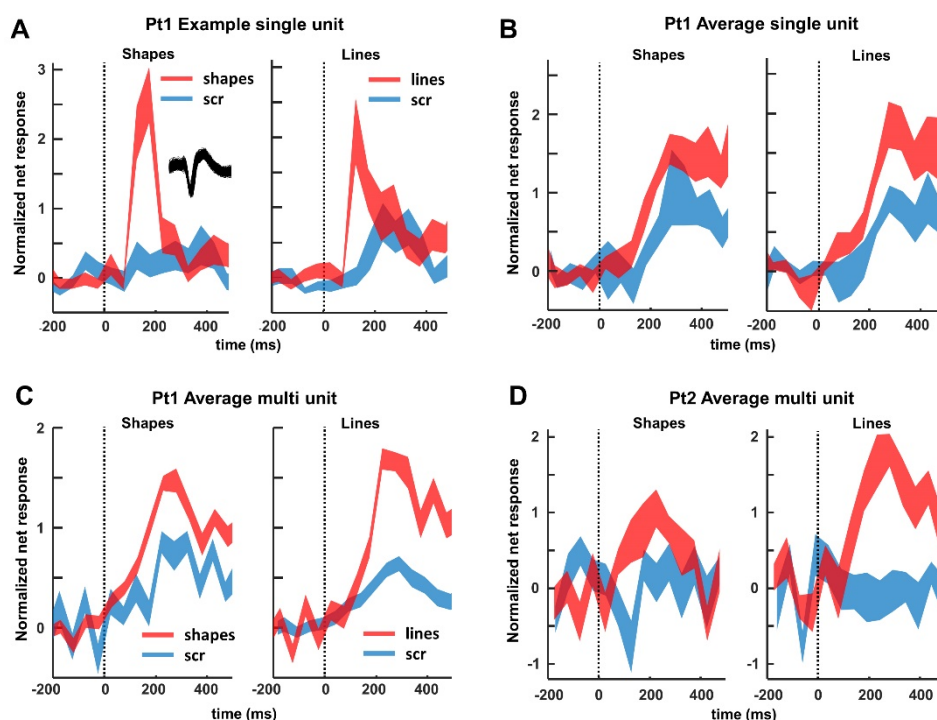

96

97   *Figure 2. Single- and multiunit responses to images of objects and scrambled controls. A.*
98   *Example neuron. Average response to intact (red) and scrambled (blue) shapes (left) and line stimuli*
99   *(right). The inset illustrates the spike waveform. B. Average single-unit responses across all visually*
100 *responsive channels in patient 1. C and D. Average multiunit responses to intact and scrambled stimuli*
101 *in patient 1 and 2, respectively, across all visually responsive channels.*

102   We recorded neuronal responses to images of objects in patient 1 in two separate sessions

103 (number of channels: 174), and detected 42 visually-responsive single units (average normalized net

104 response in Fig 2B). Entirely consistent with the fMRI results, half of these neurons (21/42) responded

105 significantly more strongly to intact than to scrambled images of objects (permutation test non-

106   scrambled versus scrambled: p <0.05; median d' index: 0.35), and no single unit showed a significant

107   preference for scrambled controls. The median response latency of these 21 selective neurons

108   (calculated on the responses to intact shapes and outlines) was 150 ms, whereas the fastest neurons

109   (percentile 10) started to respond at 75 ms after stimulus onset. However, the median selectivity

110   latency (i.e. the first bin with significant response differences between intact and scrambled images)

111   was much higher (225 ms), and no neuron started to discriminate between intact and scrambled

112   stimuli before 75 ms. We obtained highly similar results for MUA in both patients (Figure 2C and D). A

113   large number (46 out of 83) of the visually responsive channels preferred intact over scrambled shapes

114   (41 out of 71 for pt1, 5 out of 12 for patient 2; permutation test: p<0.05; median d': Pt1: 0.45, Pt2:

115   0.28). Not surprisingly, the average multi-unit response of all visually-responsive channels was greater

116   for non-scrambled stimuli than for scrambled controls (p<0.001, permutation test, Fig 2C and D).

117   When looking at the LFP signal that was recorded together with the spiking activity, virtually

118   all channels responded significantly to visual stimulation (80-120Hz, or high-gamma power intact

119   shapes versus pre-stimulus baseline ; permutation test, p <0.05; pt1: n = 164/174 or 94%; pt2: n =

120   269/285 or 94%). On average, we observed a broad-band response after stimulus onset in all four

121   conditions (permutation test, p < 0.01, corrected for multiple comparisons, Figure 3), in which the LFP

122   response to intact shapes and outlines was significantly stronger than to scrambled controls, both at

123   the level of the average high gamma power and on the great majority of the individual channels

124   (permutation test, p < 0.001; pt1: 109 /174 (63%) individual channels; pt2: 242/285 (85%) individual

125   channels). As expected, the lower frequency bands discriminated less reliably between intact and

126   scrambled shapes. Thus, SUA, MUA and LFP data clearly demonstrate that neurons in human LOC are

127   more responsive to intact shapes than to scrambled shapes, confirming and validating the results of

128   the fMRI localizer.
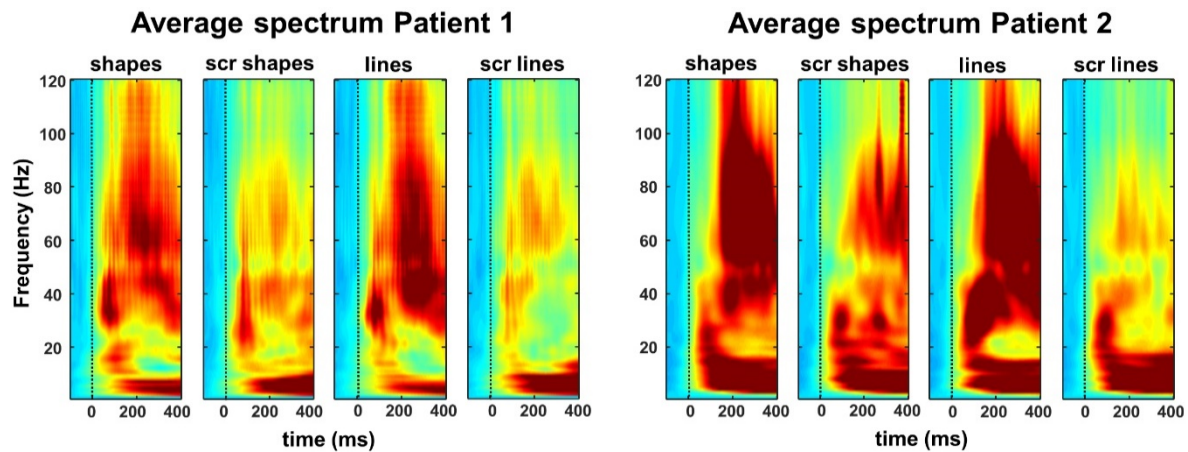
Figure 3. Time-frequency plots of the average local field potentials (LFPs) recorded in the two patients, indicating that the high-gamma (80-120 Hz) power is significantly stronger for intact shapes and outlines than for their scrambled controls.

Shape selectivity and spatial clustering

MUA recording sites were not only sensitive to image scrambling, but could also be selective for individual shapes (one-way ANOVA $p < 0.05$ in 8/46 recording sites). To quantify and visualize this shape selectivity, we ranked the intact shapes based on the MUA responses (for all 46 channels with significant selectivity for image scrambling, 6 for pt1, 40 for pt2), and calculated the average MUA response to the ranked intact shapes and to the corresponding scrambled shape images (Fig. 4A and B). Despite the fact that we did not search for selective neurons, shape selectivity was nonetheless robust, since the half-maximum response was measured for rank 17 (patient 1) and 14 (patient 2), and the least-preferred shapes even evoked inhibitory responses. No significant tuning was present for the corresponding scrambled controls (see supplementary Table S1 for linear regression slopes). The results were highly similar for the single-unit responses and for the line stimuli and their scrambled controls (supplementary Figs S1, and S2 and Table S1).

7

147
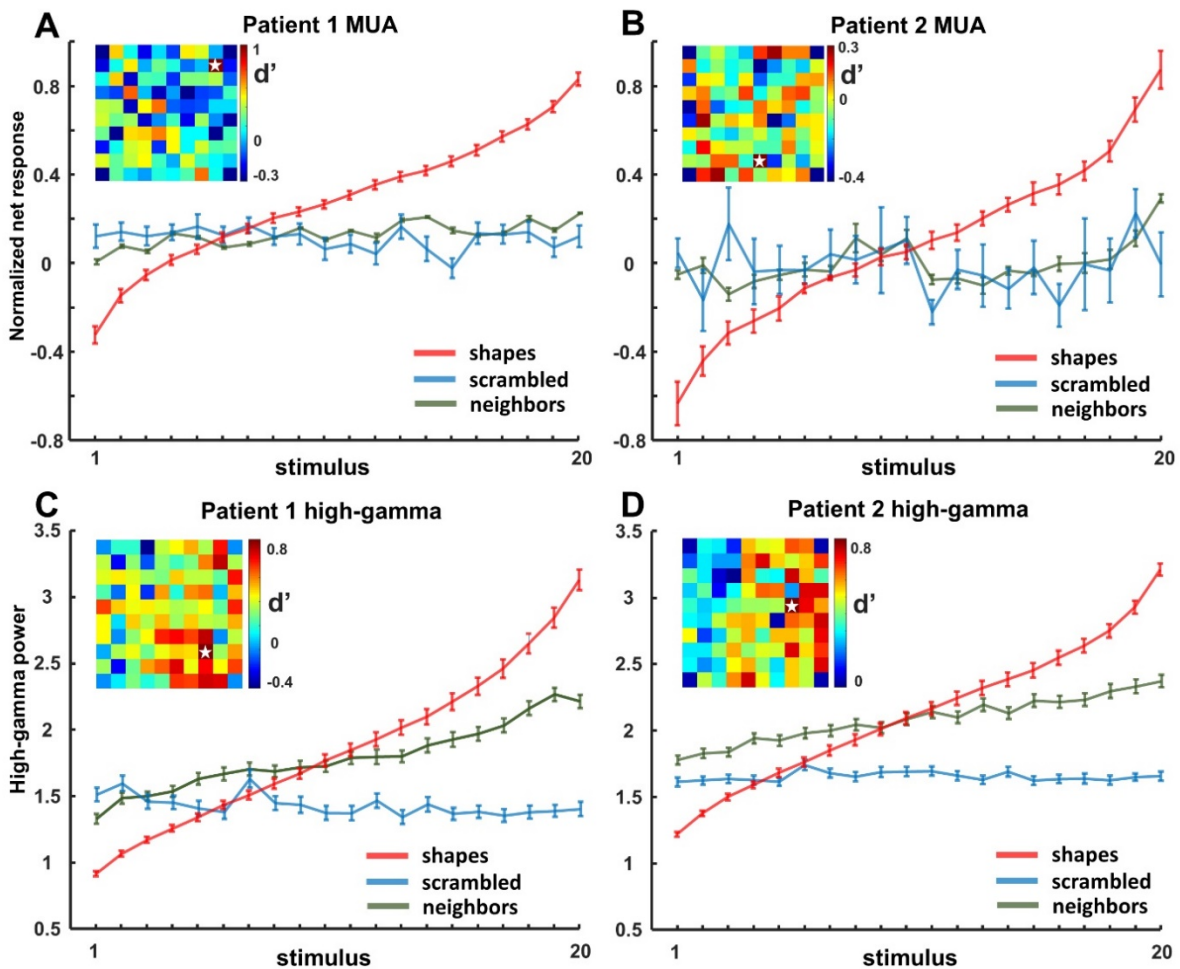
Figure 4. Ranking of shapes for multi-unit activity (MUA) and high-gamma LFP for each patient. The same ranking is applied for the neighboring channels and the corresponding scrambled control stimuli.

148
149
150
151

152   The high-gamma responses to intact shapes were equally selective (Figure 4C and D; one-way

153   ANOVA with factor *stimulus number*, for shapes: $p < 0.05$ in 15/109 for pt1; 72/242 channels for pt2).

154   The most effective intact shape elicited 3 to 4 times more high-gamma activity than the least-

155   preferred shape (half-maximum response for rank 15 in both patients), and no significant tuning was

156   present for the corresponding scrambled controls.

157   Many MUA and LFP sites were sensitive to image scrambling, but the degree of sensitivity

158   differed markedly on neighboring channels spaced a mere 400 microns apart. This unexpected spatial

159   specificity in the MUA and high-gamma responses to image scrambling became evident in the d'

160   indices mapped on the spatial layout of the array (compare for example the d' of a highly selective

161   channel indicated with a star to its neighboring channels, Fig.4A-D, insets). To quantify this spatial

162   specificity to image scrambling across the array, we calculated a 2-way ANOVA for the evoked high-

163   gamma responses for each of the 109 (pt1) or 240 (pt2) selective channels with factors *scrambling*

164   [*scrambled* vs *non-scrambled*] and *position* [neighboring position]. In the large majority of the

165   channels, the main effect of *position* (pt1: N=108/109; pt2: N=235/240) or the interaction between

166   the factors *scrambling* and *position* (pt1: N = 57/109; pt2: N=205/240) were significant ($p < 0.05$, highly

167   similar results were found for MUA).

168   We also observed a high degree of spatial clustering for shape preference across the array,

169   both at the level of MUA and at the level of high-gamma responses. For each responsive channel (the

170   center electrode), we calculated the average responses to the intact shapes on all its neighboring

171   channels based on the shape ranking of the center electrode (Fig. 4, green lines). The shape preference

172   differed markedly between each center electrode and its neighbors (Fig. 4 A-D, see Table S1),

173   indicating that the shape preference of human LOC neurons is clustered on a submillimeter scale,

174   similar to the monkey ITC (Fujita et al., 1992, Yamane et al., 2006).

175

176   **Receptive fields**

177   A fundamental characteristic of visual neurons is their receptive field (RF). To map the RF of

178   neurons in human visual cortex, we presented an intact shape at 25 positions on the screen covering

179   a 30 by 50 deg area in both hemifields. The four example neurons recorded in patient 1 (Figure 5A)

180   clearly demonstrate that the RFs were relatively large (average surface area 473 deg^2) and covered

181   both the ipsi- and the contralateral hemifield. Out of 46 visually responsive single neurons (stimulus

182   vs baseline, $p < 0.05$, permutation test), 24 (52%) responded maximally in the contralateral hemifield,

183   13 (28%) in the ipsilateral hemifield, and 9 neurons responded maximally at the midline (3 of which

184   were at the fovea). Six neurons showed bilateral responses (i.e. > 50 % of the maximal response). The

185   average RF (rightmost panel in Figure 5A) at the single-neuron level included the fovea and the

186   ipsilateral hemifield. The average RF profile was similar when determined using the high gamma

187   responses (Figure 5B): in both patients, the high gamma RF contained the center of the visual field and

188   visual responses (at > 50% of the maximum response) were present both contra- and ipsilaterally.

189   Thus, the average RF in this part of the human LOC was consistently large and bilateral.

190

191
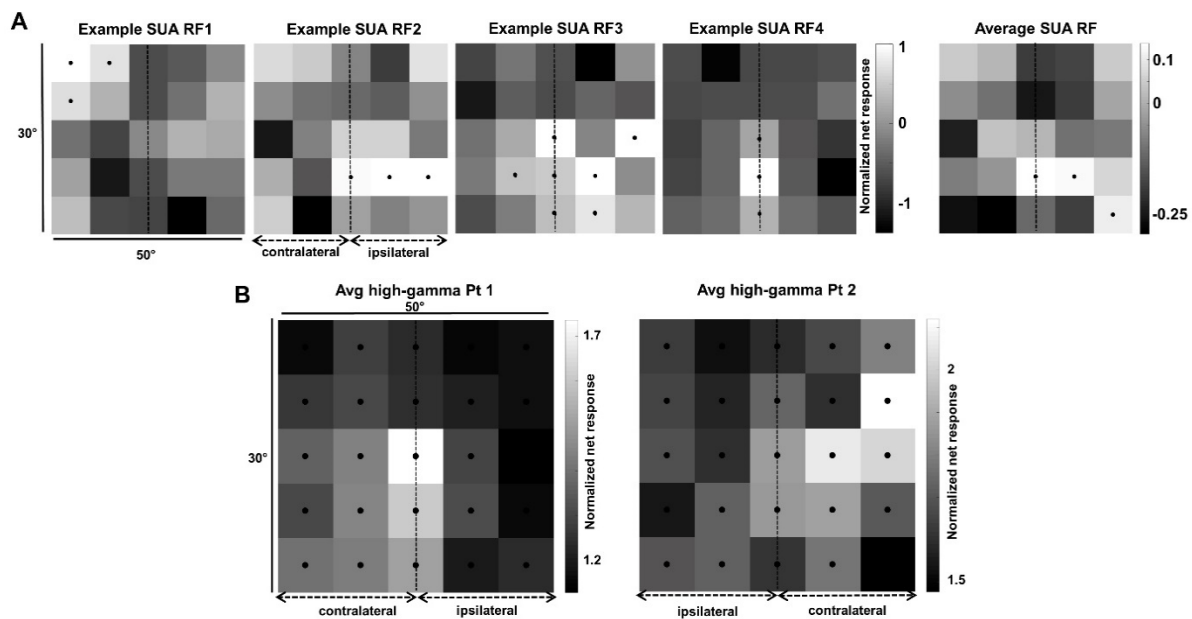
192   *Figure 5. Receptive field mapping. A. Single-unit data. The first four panels show the RFs of four*
193   *example neurons. All responses are normalized to the maximum visual response. Black dots indicate*
194   *responses higher than 50% of the maximum response (per channel). Rightmost panel: average*
195   *receptive field for all visually responsive channels. B. Average RF at the level of high-gamma responses*
196   *for patient 1 (left) and patient 2 (right).*

197

198

199   **Three-dimensional structure selectivity**

200   The previous results have addressed only neural responses to 2D shapes, but neurons in the

201   macaque ITC are also selective for 3D stimuli (Janssen et al., 2000b, Yamane et al., 2008) and several

202   human fMRI studies have suggested that the LOC is sensitive to binocular disparity (Welchman et al.,

203   2005, Georgieva et al., 2008, Moore and Engel, 2001). To investigate the selectivity of LOC neurons

204   for stereo stimuli, we ran a stereo-localizer fMRI experiment, in which blocks of stereo stimuli (curved

205   and flat surfaces at different disparities) alternated with blocks of control stimuli (the monocular

206 images presented without disparity (Durand et al., 2007, Van Dromme et al., 2015)). Figure 6B shows

207 the T-values for the contrast [*stereo*] - [*control*], plotted on the anatomical MRI and CT scans of both

208 patients with the array inserted (p<0.05, FWE corrected). The fMRI results demonstrate that the

209 microelectrode arrays, indicated by the white crosshair, were indeed implanted close to the hotspot

210 of the disparity-related fMRI activations in LOC.
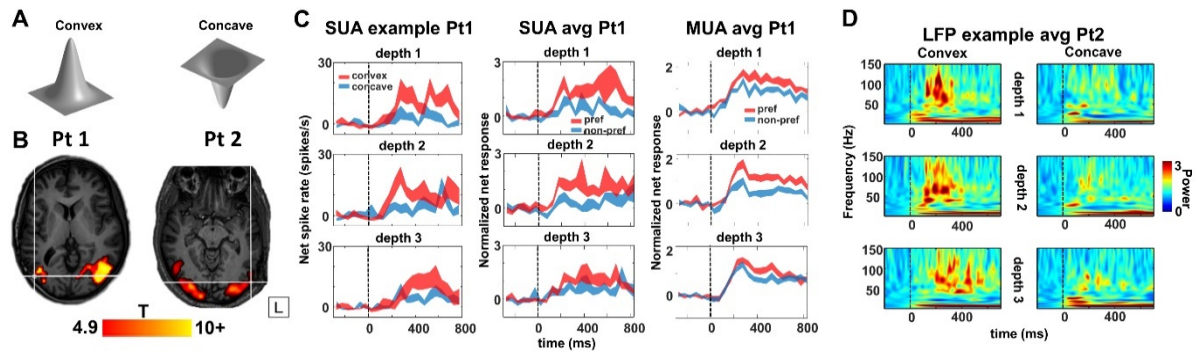
211

212 *Figure 6. Stereo experiment. A. Stimuli. B. T-values for main effects of stereo, contrast [curved*
213 *stereo + flat stereo] - [curved control + flat control], plotted on T1 weighted image. P<0.05, FWE-*
214 *corrected for multiple comparisons. Crosshair indicates the position of the Utah-array. C. Example*
215 *single neuron (left column), average single-unit responses (middle column) and average multi-unit*
216 *responses (right column) to preferred (red) and nonpreferred (blue) curved surfaces at three positions*
217 *in depth (upper row: near, middle row: center and bottom row: far). D. Time-frequency power spectra,*
218 *for example channel in patient 1, for convex and concave stimulus presentations at three positions in*
219 *depth. This site is selective for convex shapes across different positions in depth.*
220

221 We recorded neural activity in LOC during the presentation of stereo stimuli (2 recording

222 sessions) while the patients were categorizing concave and convex surfaces (Fig 6A) at different

223 positions in depth (SUA on 52 channels in Pt 1). The example neuron in Figure 6C (left panel) preferred

224 convex over concave shapes at all three positions in depth (average d' = 0.73), indicating 3D-structure

225 (i.e. higher-order disparity) selectivity. Notice that this neuron did not start to respond until 100 ms

226 after stimulus onset, and reached its peak activity only after 250 ms. In total, we recorded 39 visually

227 responsive single neurons in this test, 16 (41%) of which showed 3D-structure selectivity (i.e. a main

228 effect of *stereo* and/or a significant interaction between *stereo* and *position in depth* with no reversal

229 in selectivity (Verhoef et al., 2010)). For these 16 selective neurons, we plotted the average net

230   responses to the preferred and non-preferred 3D surfaces at each position in depth (Fig 6C middle

231   panel). This population of LOC neurons preserved its selectivity at every position in depth, as did the

232   MUA (N = 21 sites, right panel in Fig 6C). Similar to the example neuron in Figure 6C, the population

233   (SUA and MUA combined) response latency (125 ms) and the latency of the 3D-structure selectivity

234   (275 ms) were relatively long compared to previously-reported data obtained in the monkey ITC

235   (Verhoef et al., 2012, Janssen et al., 2000b). Moreover, both patients showed significant 3D-structure-

236   selective high gamma responses (15% of visually responsive channels in patient 1, 20% in patient 2,

237   example channel in Figure 6D, average high-gamma of 3D-structure-selective sites is shown for both

238   patients in Figure S3).

239   Not unlike the selectivity for image scrambling and for individual shapes, the high-gamma 3D-

240   structure preference was highly localized on individual electrodes, since recording sites with a high d'

241   (convex versus concave) were frequently located next to recording sites with a very low d'

242   (Supplementary Fig. S4). A 2-way ANOVA with factors *neighboring channel* and *stereo* (convex or

243   concave) indicated a significant clustering of the 3D-structure preference in the large majority of

244   selective channels (94 and 97% of stereo-selective neurons with a main effect of *channel* in patients 1

245   and 2, respectively, and with 2 and 5 channels, respectively, showing an interaction between channel

246   and stereo in these two patients). Since the high-gamma response correlates with population spiking

247   activity (Liu and Newsome, 2006, Premereur et al., 2012), these results indicate clustering of the 3D-

248   structure preference in human LOC, consistent with previous findings in monkey ITC (Verhoef et al.,

249   2012).

250

251

252

253

254

Discussion

255

256   We present the first report of intracortical recordings in SUA, MUA and LFP activity in human LOC

257   using microelectrode arrays. Our 96-electrode array with an interelectrode spacing of 0.4 mm allowed

258   extensive neuronal recordings in human visual cortex with an unprecedented spatiotemporal

259   resolution. Our experiments confirm the robust sensitivity of LOC neurons to image scrambling, as

260   predicted by fMRI, reveal significant 2D-shape and 3D-structure selectivities at the level of SUA, MUA

261   and high-gamma responses, and provide the first RF maps of individual LOC neurons. Moreover, our

262   data furnish new and crucial evidence concerning the microarchitecture of LOC, in that the shape

263   preference differed drastically between neighboring electrodes spaced a mere 400 microns apart.

264   Our approach using a microelectrode array has several advantages compared to previous

265   electrophysiological studies in humans. Subdural grids with contact points measuring several

266   millimeters (Yoshor et al., 2007) sample neural activity over a wide area, whereas we used

267   intracortical microelectrodes with sharp tips spaced just 400 microns apart, so that a single row of 10

268   electrodes occupied a stretch of cortex measuring only 3.6 mm. Furthermore, the microelectrode

269   array allowed us to simultaneously record neural activity on 96 microelectrodes, compared to

270   recordings on only two microelectrodes in (Self et al., 2016). Finally, the spatial arrangement of the

271   microelectrode array (10 by 10 electrodes) also allowed us to investigate the microarchitecture of

272   human visual cortex at the scale of cortical columns. It should also be noted that our recording sites

273   were located near the entry point of one of the depth electrodes and were, in retrospect, not part of

274   the epileptogenic zone.

275   Ever since the original publication by (Kourtzi and Kanwisher, 2000), numerous studies have used

276   the LOC localizer [intact shapes – scrambled shapes] to identify shape-sensitive regions in human

277   visual cortex. However, the actual underlying neural selectivity has never been revealed. An extensive

278   body of work has employed visual adaptation, observed via fMRI activation, as an indirect

279   measurement of neuronal shape selectivity in humans (e.g. (Grill-Spector and Malach, 2001)), but the

280   interpretation of these effects and their relation to neural selectivity at the single-cell level remain

13

281   controversial (Sawamura et al., 2006). Here, we not only confirmed the strong effect of image

282   scrambling on SUA, MUA and high-gamma responses in LOC, but we also revealed significant response

283   differences for intact shapes, i.e. shape selectivity, at the level of single neurons, as previously shown

284   in the macaque ITC (Logothetis and Sheinberg, 1996, Tanaka, 1996). A bilateral lesion of LOC produces

285   a profound deficit in shape recognition (Goodale et al., 1991, James et al., 2003, Westwood and

286   Goodale, 2011), similar to ITC lesions in monkeys (Cowey and Gross, 1970, Britten et al., 1992, Dean,

287   1976, Gross, 1994, Dean, 1979), and Transcranial Magnetic Stimulation over LO also impairs shape

288   discrimination (Chouinard et al., 2017). Our data support the notion that these deficits arise from a

289   loss of shape-selective neurons in LOC.

290   A substantial fraction of our MUA and LFP recording sites showed significant shape tuning –

291   possibly as strong as in the monkey ITC (De Baene and Vogels, 2010) – indicating that shape preference

292   may be localized within the LOC. In addition, the fixed arrangement of the microelectrodes, spaced

293   400 microns apart, allowed assessing the spatial organization of sensitivity to image scrambling and

294   of the shape selectivity at a high spatial resolution. Our observation that the shape preference

295   changed markedly over the extent of 400 microns is in line with previous studies in the macaque ITC

296   demonstrating considerable clustering for shape features. Fujita et al ((Fujita et al., 1992)) showed

297   that ITC neurons with similar shape selectivities are organized vertically across the cortical thickness,

298   and (Tsunoda et al., 2001) used intrinsic optical imaging to highlight patches of activation elicited by

299   specific object images spaced 0.4 to 0.8 mm apart. Thus, our results are highly consistent with previous

300   studies in the ITC of macaque monkeys.

301   The spatially-restricted nature of high-gamma responses we measured in LOC is consistent with

302   previous studies in visual cortex indicating that the higher frequency bands of the LFP signal

303   correspond with MUA (Goense and Logothetis, 2008, Liu and Newsome, 2006, Logothetis et al., 2001,

304   Premereur et al., 2012) and originate from a small region of cortex measuring a few hundred microns

305   in extent (Katzner et al., 2009). However, studies in auditory cortex reported considerable volume

306   conduction – even in the high-gamma band of the LFP signal – over several millimeters of cortex

307 (Kajikawa and Schroeder, 2011). Although our data do not allow us to fully resolve this controversy, it

308 should be noted that our spatially-selective recordings were obtained during an active fixation task,

309 where no influence of anesthetics was possible, in contrast to the Kajikawa and Schroeder study. It

310 should also be noted that although we recorded SUA in one patient, we were able to confirm our

311 findings with MUA and high-gamma responses in both patients.

312 Our data also shed light on the RF properties of LOC neurons. Although we did not obtain sufficient

313 data for an exhaustive RF description, a few conclusions seem to be warranted. The average RF size in

314 LOC was large (473 deg^2), and a considerable fraction of LOC neurons responded to stimuli presented

315 in the ipsilateral hemifield. A previous study in human early visual cortex reported that the RF

316 measured with high-gamma responses is even more restricted than that measured with MUA (Self et

317 al., 2016). Thus, our observation that LOC sites frequently exhibit bilateral SUA, MUA and high-gamma

318 responses is interesting in view of the comparison between the human LOC and monkey ITC areas

319 (see below). Future studies will have to investigate the RF profile of LOC neurons in more detail.

320 To our knowledge, we also provide the first evidence for 3D-structure selectivity defined by

321 binocular disparity in human visual cortex. A number of recording sites showed differential responses

322 to convex and concave surfaces (composed of the same monocular images), across different positions

323 in depth, indicative of higher-order disparity or 3D-structure selectivity. Similar to the selectivity for

324 image scrambling and that for individual shapes, the 3D-structure preference was highly localized on

325 individual electrodes, since recording sites with strong selectivity were frequently located next to

326 recording sites with a very low selectivity. A large number of studies (Janssen et al., 2001, Janssen et

327 al., 2003, Janssen et al., 1999, Janssen et al., 2000b, Janssen et al., 2000a, Yamane et al., 2008) have

328 investigated 3D-structure selectivity in the macaque anterior ITC (area TE). More recently, Verhoef et

329 al. showed clustering of the MUA selectivity for 3D structure in area TE using identical stimuli (Verhoef

330 et al., 2012), and microstimulation of these clusters could predictably alter the perceptual report of

331 the animal in a 3D-structure categorization task. Hence, the 3D-structure selectivity we observe here

332 has also been described in the macaque ITC. Moreover, patient DF (Read et al., 2010), who suffered

15

333   bilateral damage to LOC, was impaired in using the relative disparity between features at different

334   locations, although 3D-structure categorization was not tested.

335   One major, outstanding question relates to the possible homologies between the different

336   subparts of human LOC and monkey ITC areas TEO and TE (Orban et al., 2014). Although a single study

337   cannot resolve this homology question, several observations we made are highly relevant in this

338   respect. Shape-selective responses can be observed in TEO and in TE. However, the robust 3D-

339   structure selectivity we observed was previously described in the more anterior part of area TE in

340   macaques (Janssen et al., 2000b), but is virtually absent in macaque area TEO (Alizadeh et al., 2018).

341   Moreover, the large and frequently bilateral RFs we observed in human LOC are more consistent with

342   TE than with TEO (Hikosaka, 1999). Detailed mapping of receptive fields (Boussaoud et al., 1991,

343   Kobatake and Tanaka, 1994) and stimulus reduction during single-unit recordings (Tanaka et al., 1991)

344   will clarify in greater detail the relationship between this part of the LOC and the monkey ITC areas.

345   Overall, the similarities between the human LOC and the (more anterior part of) monkey ITC were

346   very apparent. In both species, neurons are sensitive to image scrambling (Vogels, 1999) and shape-

347   selective; shape preference is clustered; the RFs are large and include the fovea (Op de Beeck et al.,

348   2001), and neurons preserve their 3D structure preferences across position in depth (Janssen et al.,

349   2000b). The only possible discrepancy between our results in the human LOC and previous studies in

350   monkey ITC may reside in the latencies of the neuronal response. When tested with images of objects,

351   the MUA became selective only after 125 ms, and the response and selectivity latency for 3D stimuli

352   equaled 125 and 225 ms, respectively. In contrast, macaque ITC neurons can signal shape differences

353   starting at 70-80 ms after stimulus onset and at 80-100 ms for 3D stimuli (Janssen et al., 2000b)).

354   However, our results are in line with previous studies in the human medial temporal lobe – which is

355   downstream from LOC – reporting latencies of 300 ms (Quiroga et al., 2005, Kreiman et al., 2000b).

356   However, neuronal latencies are highly influenced by the number of stimulus repetitions, therefore a

357   higher number of selective recording sites and a higher number of trials may have yielded shorter

16

358   latencies in our experiments. More detailed measurements in the two species in areas where the

359   homology is clearly established (e.g. V1) are undoubtedly necessary.

360

361   **Materials and Methods**

362   Two patients (Pt2, 28 y.o. female; Pt1, 44 y.o. male) with refractory epilepsy underwent invasive

363   intracranial recordings with the use of depth electrodes to delineate the epileptogenic zone. During

364   this procedure microelectrode arrays were implanted in the left (patient 1) and right (patient 2) lateral

365   occipital complex. Informed consent from the patients and local ethical board approval was obtained

366   for this procedure (study protocol S 53126).

367

368   fMRI

369   *Stimuli*

370   The stimuli were projected from a liquid crystal display projector (Barco Reality 6400i, 1024 x 768

371   pixels, 60-Hz refresh rate) onto a translucent screen positioned in the bore of the magnet (57 cm

372   distance). The patients viewed the stimuli through a mirror tilted at 45° and attached to the head coil.

373   *LO Localizer*: The LO localizer stimuli were images measuring 300 × 300 pixels. We used grayscale

374   images and line drawings of familiar objects (20 images and 20 line drawings), as well as scrambled

375   versions of each set (Fig. 1A) (Kourtzi et al., 2003). The scrambled images were created by dividing the

376   intact images into a 20 × 20 square grid and randomizing the positions of each of the resulting squares.

377   The grid lines were present in both the intact and the scrambled images. The overall size of the stimuli

378   measured 7° in visual angle and each stimulus was presented for 1000 ms.

379   *Stereo Localizer*: The stimulus set consisted of random-dot stereograms in which the depth was

380   defined by horizontal disparity (dot size 0.08°, dot density 50%, vertical extent 5.5°), and were

381   presented on a gray background. All stimuli were generated using MATLAB (R2010a, MathWorks) and

382   were gamma-corrected. We used a 2 by 2 design with factors *curvature* (curved vs flat) and *disparity*

17

383   (stereo vs control), as described in (Durand et al., 2007, Joly et al., 2009, Van Dromme et al., 2016, Van

384   Dromme et al., 2015). The stereo-curved condition consisted of three types of smoothly-curved depth

385   profiles (1, 1/2, or 1/4 vertical sinusoidal cycle) together with their antiphase counterparts obtained

386   by interchanging the right and left monocular images (disparity amplitude within the surface: 0.5°).

387   Each of the six depth profiles was combined with one of four different circumference shapes and

388   appeared at two different positions in depth (mean disparity + or − 0.5°), creating a set of 48 curved

389   surfaces. In the stereo-flat condition, flat surfaces (using the same four circumference shapes) were

390   presented at 12 different positions in depth, such that the disparity content (the sum of all disparities)

391   was identical to that in the stereo curved condition. Finally, the control conditions (stereo-control and

392   flat-control) consisted of the presentation of one of the monocular images (either belonging to one of

393   the stereo-curved stimuli or to one of the stereo-flat stimuli) to both eyes simultaneously. Each control

394   condition consisted of exactly the same monocular images as the corresponding stereo condition,

395   hence the binocular input was identical in the stereo conditions and in the control conditions. The

396   overall size of the stimuli measured 5.6° in visual angle and each stimulus was presented for 1000 ms.

397   Dichoptic presentation of the stimuli was achieved by means of red/green filter stereo glasses worn

398   by the patient.

399

400   *Data collection*

401   Scanning was performed on a 3-T MR scanner (Achieva dstream, Philips Medical Systems, Best, The

402   Netherlands) located at the University Hospitals Leuven. Functional images were acquired using

403   gradient-echoplanar imaging with the following parameters: 52 horizontal slices (2 mm slice thickness;

404   0.2 mm gap; multiband acquisition), repetition time (TR) 2 s, time of echo (TE): 30 ms, flip angle: 90°,

405   112 * 112 matrix with 2 x2 mm in-plane resolution, and sensitivity-enhancing (SENSE) reduction factor

406   of 2. The 25 slices of a volume covered the entire brain from the cerebellum to the vertex. A three-

407   dimensional (3D) high-resolution (18181.2) T1-weighted image covering the entire brain was acquired

408   in the beginning of the scanning session and used for anatomical reference (TE/TR 4.6/9.7 ms;

409   inversion time, 900 ms; slice thickness, 1.2 mm; 256 * 256 matrix; 182 coronal slices; SENSE reduction

410   factor 2.5). The single scanning session lasted 60 min.

411   *CT:* A computed tomography (CT) scan (Siemens, 1mm slice thickness, 120kV, Dose length product of

412   819mGy.cm) was performed two hours after electrode placement to verify the location of the

413   microelectrode array.

414   *LO Localizer*: Stimuli (shapes, line stimuli, scrambled shapes, scrambled line stimuli, fixation only, Fig.

415   1A) were presented in blocks of 24 s except for the fixation condition (20 s), each block was repeated

416   4 times in a run, creating runs of 464 s. Individual stimuli were presented for 1000 ms (ISI=0; fixation

417   time: 200 ms).

418   *Stereo Localizer*: Stimuli (curved stereo, flat stereo, curved control, flat control, fixation only, Fig. 1B)

419   were presented in blocks of 24 s, and each block was repeated 4 times in a run, creating runs of 480

420   s. Individual stimuli were presented for 1000 ms (interstimulus interval = 0 ms; fixation time = 200

421   ms). 12 functional volumes were acquired for every block (or condition, each 24 s long) and these

422   were embedded in a time series of 222 volumes (444 s).

423

424   *Data analysis*

425   Data analysis was performed using the SPM12 software package (Wellcome Department of Cognitive

426   Neurology, London, UK) running under MATLAB (The Mathworks, Natick, MA). The preprocessing

427   steps involved *1*) realignment of the images, *2*) coregistration of the anatomical image and the mean

428   functional image. Before further analysis, the functional data were smoothed with an isotropic

429   Gaussian kernel of 5 mm. To determine the exact location of the Utah array, the CT scan was

430   coregistered with the anatomical image using SPM12 software.

19

431 *LO Localizer*: To localize areas responding more strongly to the presentation of objects versus

432 scrambled controls, we calculated the contrast [shapes + outlines] - [scrambled shapes +scrambled

433 outlines], at p < 0.05, FWE corrected.

434 *Stereo*: To identify regions sensitive to binocular disparity, we calculated the main effect of *stereo*:

435 [curved stereo + flat stereo] - [curved control + flat control], at p < 0.05, FWE corrected.

436 Electrophysiology

437 We implanted a 96-channel microelectrode array with 1.5 mm electrode length in patient 1 and with

438 1 mm electrode length in patient 2; electrode spacing measured 400 microns (4 x 4 mm; Blackrock

439 Microsystems, UT, USA). The array was implanted through a burr hole over the occipitotemporal

440 cortex, used for depth electrode placement, according to the manufacturer's protocol with a

441 pressurized inserter wand. These microelectrodes were used clinically for advanced epilepsy

442 monitoring (study protocol S 53126).

443

444 *Stimuli*

445 All stimuli were presented by means of a custom-made stereoscope. Images from two LCD monitors

446 were presented to the two eyes with the use of customized mirrors at a viewing distance of 56 cm (1

447 pixel = 0.028°). Continuous eye-movement tracking (left eye, 120Hz; ISCAN, MA, USA), ensuring

448 fixation in an electronically defined window (3*3 degrees), was performed throughout the

449 experiment. Trials in which the patients did not maintain fixation were aborted.

450 *LO Localizer:* The same stimulus set as in the fMRI experiment was used. The the stimuli presented in

451 the stereoscope were 8.5 deg in size. After a brief period of fixation (200 ms), the stimulus was

452 presented for 500 ms, followed by an interstimulus interval of 100 ms. In the LO localizer, no disparity

453 was present in the stimuli.

454 *Receptive field mapping*: To map the RF, a single non-scrambled shape (8.5 deg) was presented at 25

455 different positions in the visual field, covering 50 degrees horizontally and 30 degrees vertically, during

456 passive fixation.

457 *Stereo test:* We presented concave and convex surfaces at three different positions in depth (near, at

458 the fixation plane, and far, Fig. 1C) at the fixation point while monitoring the position of the left eye.

459 To avoid monocular depth cues, the disparity (disparity amplitude: 0.25 deg) varied only along the

460 surface of the shape, while the circumference of the shape was kept at a constant disparity (+0.25

461 deg, 0 deg or -0.25 deg disparity), as in (Verhoef et al., 2010, Verhoef et al., 2012). The patients had

462 to categorize the 3D structure of the stimulus (concave or convex, 100% disparity coherence)

463 independently of the position in depth by means of a button press after stimulus offset (1000 ms of

464 stimulus presentation time), as in (Verhoef et al., 2010). An auditory tone provided feedback after

465 every successfully completed trial. Both patients performed at more than 90% correct.

466

467 *Data Collection*

468 Data were collected using a digital headstage (Blackrock Microsystems, UT, USA) connected to a 128-

469 channel neural signal processor (Blackrock Microsystems, UT, USA). For LFP recordings, the signal was

470 filtered with a digital low-pass filter of 125 Hz, and LFP signals were recorded continuously (sampling

471 frequency: 1000 Hz). Single- and multi-unit signals were high-pass filtered (750 Hz). A multi-unit

472 detection trigger was set at a level of 95% of the signal's noise. All spike sorting was performed offline

473 (Offline Sorter 4, Plexon, TX, USA).

474

475 *Data analysis*

476 Data analysis was performed using custom-written Matlab (the MathWorks, MA, USA) software.

477 *Spike rate analysis:* For every channel, we calculated the net spike rate by subtracting the

478 average baseline activity from the spike rate. Spike rate was further normalized by dividing the net

479 spike rates by the average spike rate for the best condition (50-300 ms after stimulus onset) for each

480 channel. Statistics were performed using permutation tests, where real data were randomly

481 distributed over all the different conditions 1000 times. The differences between two conditions were

482 calculated for every permutation, and compared with the actual difference between conditions. The

21

483 latency of the spiking activity for visually-responsive channels was defined as the first of two

484 consecutive 50 ms bins with a spike rate higher than the average baseline plus 2 standard errors. The

485 selectivity latency was defined as the first of two consecutive 50 ms bins with a spike rate for the

486 preferred condition higher than the average spike rate for the non-preferred condition plus 2 standard

487 errors.

488 *LFP analysis:* For every trial, the time-frequency power spectrum was calculated using Morlet's

489 wavelet analysis techniques (Tallon-Baudry and Bertrand, 1999), with a spectro-temporal resolution

490 equal to 7, after filtering with a 50 Hz notch filter (FieldTrip Toolbox, Donders Institute, The

491 Netherlands (Oostenveld et al., 2011)). This method provides a better compromise between time and

492 frequency resolution compared to methods using Fourier transforms (Sinkkonen et al., 1995, Tallon-

493 Baudry et al., 1997). To remove any filter artifacts at the beginning and end of the trial, the first and

494 last 100 ms of each trial were discarded. Power was normalized per trial by dividing the power trace

495 per frequency by the average power for this frequency in the 100 ms interval before stimulus onset.

496 To exclude trials containing possible artifacts in the LFP recordings, maximum values of the continuous

497 LFP signal were determined and trials with maximum values above the 95th percentile were removed.

498 Furthermore, the data set was split in two, and all population analyses were repeated for both halves

499 of the data independently, to check for consistency. We analyzed the LFP power in the high frequency

500 bands (high-gamma): 80-120 Hz. Lowest frequencies had to be excluded from our analyses, as our

501 trials were maximally 1 s long. All statistics on LFP data were obtained using permutation tests as

502 described for spiking activity. The latency of the LFP response per frequency band was defined as the

503 first of five consecutive timestamps (in ms) in which the average power minus 2 standard errors was

504 higher than 1 (= average power of the normalized baseline). The LFP-latency for selectivity between

505 conditions was defined as the first of two consecutive samples in which the average power for

506 condition *A* minus 2 standard errors was higher than the average power for condition *B*.

507 *D-prime:* d' statistics were calculated as:

508        $d' = (\mu_{Pref} - \mu_{NonPref}) / \sigma$

509   Here μ_{Pref} and $\mu_{NonPref}$ denote the mean responses to the preferred and the non-preferred condition

510   (e.g. non-scrambled versus scrambled), respectively, and

511 $\sigma = \sqrt{(\sigma2_{Pref} + \sigma2_{NonPref})/ 2}$

512   is the pooled variance of the two response distributions. This measure differs from those used

513   in previous studies (Frien and Eckhorn, 2000, Frien et al., 2000, Liu and Newsome, 2006) in that it

514   explicitly takes into account the trial-by-trial variability of the response (Siegel and Konig, 2003).

515   To estimate the spatial extent of selectivity observed in the MUA and high-gamma band over

516   the array, we determined for each visually responsive channel its immediate neighbors (i.e. either 8

517   channels, for recording channels which were not located on the edge of the array, or 5 channels for

518   edge electrodes). We calculated a two-way ANOVA with factors *scrambling* (scrambled vs non-

519   scrambled) and *position* for each channel individually. Significance was tested using a p-value of 0.05.

520   *Ranking: T*o investigate the MUA and high-gamma responses to individual stimuli, we applied

521   a ranking technique in which individual non-scrambled stimuli were ranked based on the electrode's

522   average spiking activity and high-gamma power evoked by the stimuli, then the same ranking was

523   applied to the individual scrambled control stimuli. To investigate differences between rankings, a

524   linear regression was performed, and a 95% confidence interval was used to determine significant

525   differences between regression coefficients or intercepts. Finally, the same ranking technique was

526   used to investigate the spatial specificity of the shape selectivity: we ranked the non-scrambled stimuli

527   for each electrode based on the spiking activity and high-gamma responses, and this same ranking

528   was then applied to the responses of all neighboring channels separately. We then averaged the spike

529   rate and gamma responses for the ranked data of the neighboring channels to determine whether the

530   shape preference was preserved at neighboring channels. Differences in ranking were investigated

531   using a linear fit as described above.

532   *Receptive fields.* The average single-unit activity and high gamma power were calculated

533   during stimulus presentation for each stimulus-position, and filtered with a Gaussian (sigma: 0.5).

534   To calculate receptive field size, we constructed RF maps by interpolating the neuronal responses

535   between all positions tested across the 50*30 degrees display area, and then calculating the number
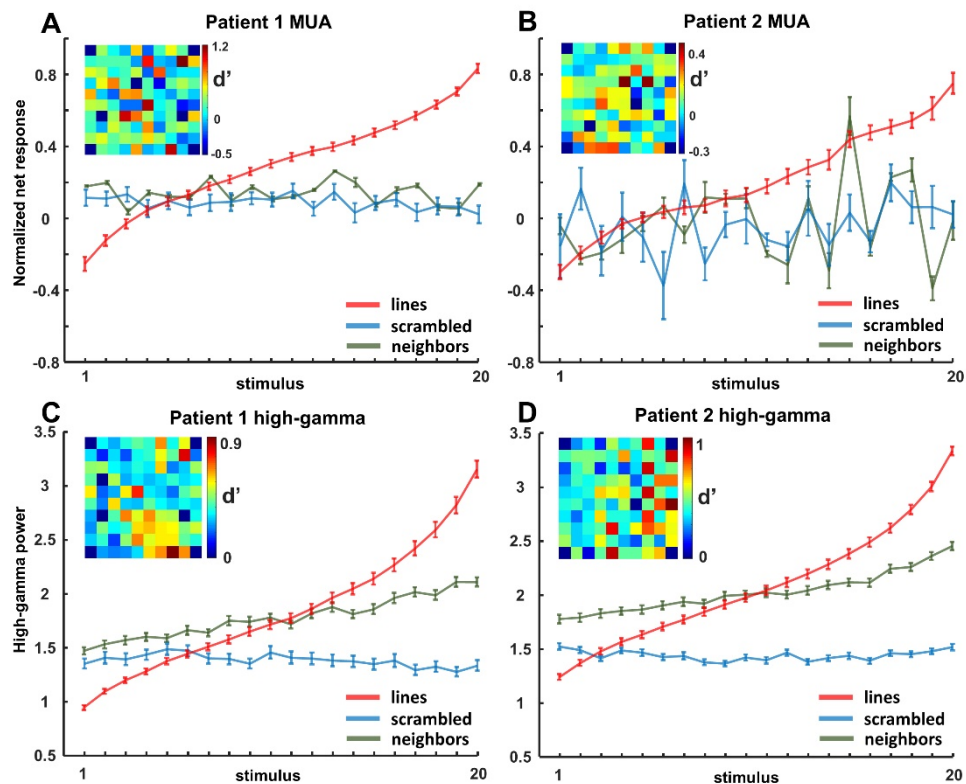
536   of pixels in the RF map with a response higher than 50% of the maximum response.

537 **Supplementary Information**
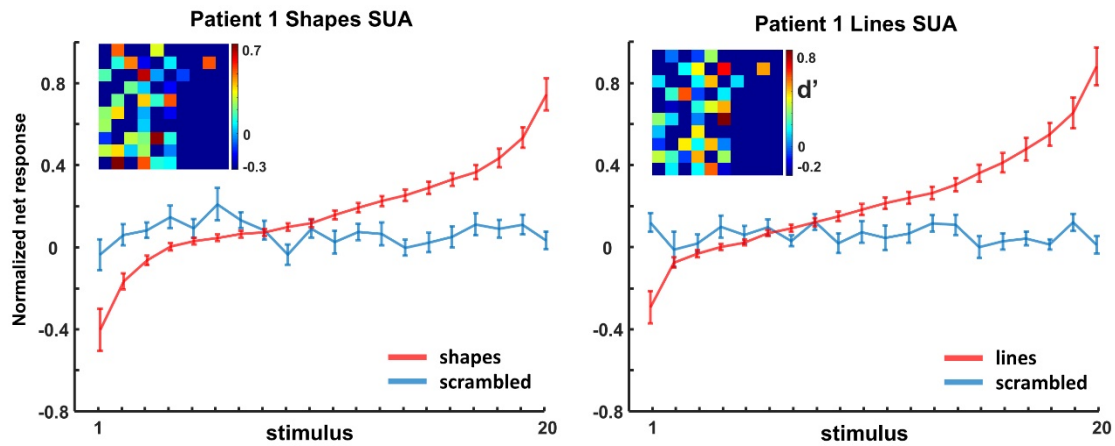
538

539 *Figure S1. Ranking analyses of shapes and lines for single-unit activity (SUA) in patient 1. The same*
540 *ranking is applied for the corresponding scrambled control stimuli.*
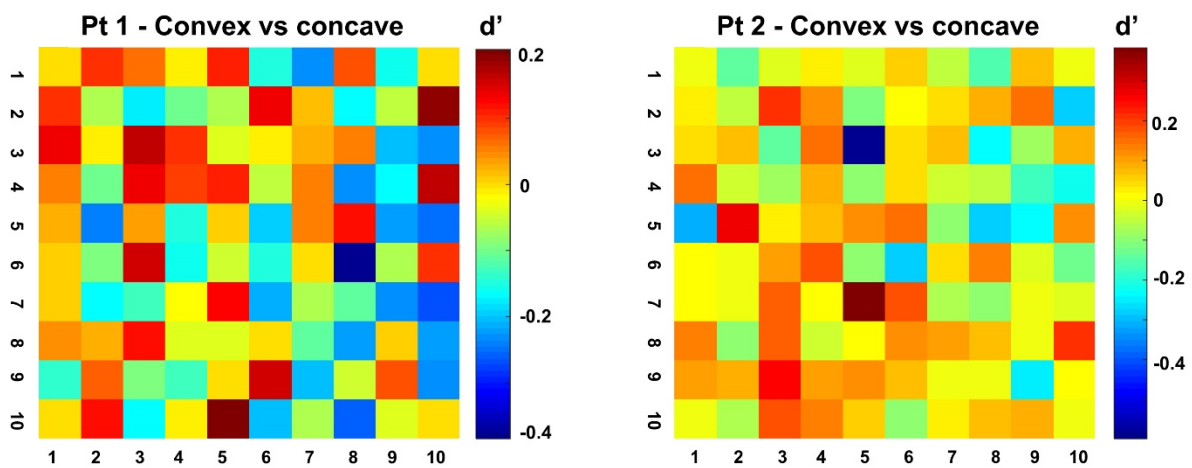
541

542

543 *Figure S2. Ranking of lines for multi-unit activity (MUA) and high-gamma LFP for both patients. The*
544 *same ranking is applied for the neighboring channels and the corresponding scrambled control*
545 *stimuli.*

25
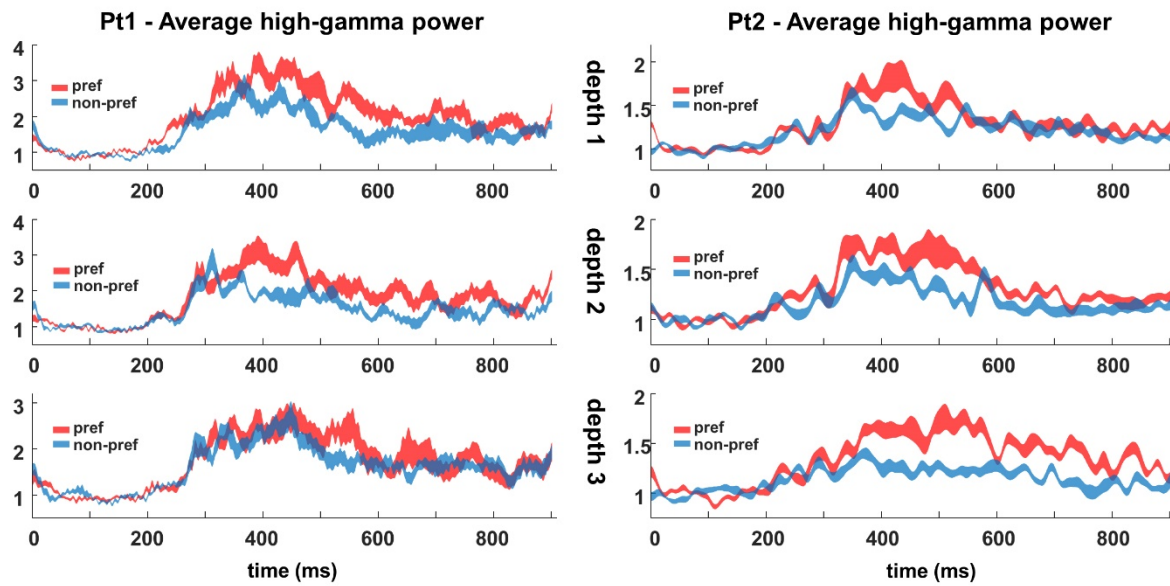
Figure S3. Average high-gamma of 3D-structure-selective sites for each patient. Preferred vs non-preferred shapes.

Figure S4. d' values of high-gamma responses for the two patients across the array. High-gamma 3D-structure preference was highly localized on individual electrodes, since recording sites with a high d' (convex versus concave) were frequently located next to recording sites with a low d'.

	Patient 1			Patient 2	
	SUA	*MUA*	*LFP*	*MUA*	*LFP*
Shapes	0.0404 (0.0337, 0.047)	0.049 (0.0448, 0.0531)	0.1015 (0.0932, 0.1097)	0.0623 (0.0561, 0.0685)	0.0892 (0.0834, 0.095)
Applied ranking for scr_shapes	-0.0008* (-0.0058, 0.0042)	-0.0026* (-0.0064, 0.0011)	-0.0077* (-0.0129, -0.0026)	-0.0005* (-0.0098, 0.0087)	0.0002* (-0.0027, 0.0031)
Applied ranking for neighbors	/	0.0072* (0.0043 - 0.0101)	0.041* (0.0362 - 0.0458)	0.0082* (0.001 - 0.0153)	0.0285* (0.026 - 0.0309)
Lines	0.0443 (0.038, 0.0507)	0.0468 (0.0431, 0.0505)	0.0974 (0.0867, 0.108)	0.0469 (0.0432, 0.0506)	0.0919 (0.082, 0.1018)
Applied ranking for scr_lines	-0.0009* (-0.289, -0.0047)	0.1483* (-0.0028, -0.0056)	-0.0059* (-0.0094, -0.0024)	0.0073* (-0.0047, 0.0194)	-0.0005* (-0.0043, 0.0034)
Applied ranking for neighbors	/	-0.0006* (-0.0057 - 0.0045)	0.0312* (0.0279 - 0.0346)	0.0007* (-0.0116 - 0.0256)	0.0305* (0.0262 - 0.0347)

555

556 *Table S1. Slope of regression lines with 95% confidence interval for shapes and lines. The same*

557 *ranking was applied for the scrambled versions of the stimuli and for their neighboring channels*

558 *respectively. * Indicates significant ranking difference.*

27

566

567   **Declaration of Interests**

568   The authors declare no competing interests

569

570

References

AFLALO, T., KELLIS, S., KLAES, C., LEE, B., SHI, Y., PEJSA, K., SHANFIELD, K., HAYES-JACKSON, S., AISEN, M., HECK, C., et al. 2015. Neurophysiology. Decoding motor imagery from the posterior parietal cortex of a tetraplegic human. *Science,* 348**,** 906-10.

ALIZADEH, A. M., VAN DROMME, I. C. & JANSSEN, P. 2018. Single-cell responses to three-dimensional structure in a functionally defined patch in macaque area TEO. *J Neurophysiol,* 120**,** 2806-2818.

ALLISON, T., PUCE, A., SPENCER, D. D. & MCCARTHY, G. 1999. Electrophysiological studies of human face perception. I: Potentials generated in occipitotemporal cortex by face and non-face stimuli. *Cereb Cortex,* 9**,** 415-30.

ARROYO, S., LESSER, R. P., GORDON, B., UEMATSU, S., JACKSON, D. & WEBBER, R. 1993. Functional significance of the mu rhythm of human cortex: an electrophysiologic study with subdural electrodes. *Electroencephalogr Clin Neurophysiol,* 87**,** 76-87.

BOUSSAOUD, D., DESIMONE, R. & UNGERLEIDER, L. G. 1991. Visual topography of area TEO in the macaque. *J Comp Neurol,* 306**,** 554-75.

BRITTEN, K. H., NEWSOME, W. T. & SAUNDERS, R. C. 1992. Effects of inferotemporal cortex lesions on form-from-motion discrimination in monkeys. *Exp Brain Res,* 88**,** 292-302.

CHOUINARD, P. A., MEENA, D. K., WHITWELL, R. L., HILCHEY, M. D. & GOODALE, M. A. 2017. A TMS Investigation on the Role of Lateral Occipital Complex and Caudal Intraparietal Sulcus in the Perception of Object Form and Orientation. *J Cogn Neurosci,* 29**,** 881-895.

COWEY, A. & GROSS, C. G. 1970. Effects of foveal prestriate and inferotemporal lesions on visual discrimination by rhesus monkeys. *Exp Brain Res,* 11**,** 128-44.

DE BAENE, W. & VOGELS, R. 2010. Effects of adaptation on the stimulus selectivity of macaque inferior temporal spiking activity and local field potentials. *Cereb Cortex,* 20**,** 2145-65.

DEAN, P. 1976. Effects of inferotemporal lesions on the behavior of monkeys. *Psychol Bull,* 83**,** 41-71.

DEAN, P. 1979. Visual cortex ablation and thresholds for successively presented stimuli in rhesus monkeys: II. Hue. *Exp Brain Res,* 35**,** 69-83.

DURAND, J. B., NELISSEN, K., JOLY, O., WARDAK, C., TODD, J. T., NORMAN, J. F., JANSSEN, P., VANDUFFEL, W. & ORBAN, G. A. 2007. Anterior regions of monkey parietal cortex process visual 3D shape. *Neuron,* 55**,** 493-505.

FRIED, I., MACDONALD, K. A. & WILSON, C. L. 1997. Single neuron activity in human hippocampus and amygdala during recognition of faces and objects. *Neuron,* 18**,** 753-65.

FRIEN, A. & ECKHORN, R. 2000. Functional coupling shows stronger stimulus dependency for fast oscillations than for low-frequency components in striate cortex of awake monkey. *Eur J Neurosci,* 12**,** 1466-78.

FRIEN, A., ECKHORN, R., BAUER, R., WOELBERN, T. & GABRIEL, A. 2000. Fast oscillations display sharper orientation tuning than slower components of the same recordings in striate cortex of the awake monkey. *Eur J Neurosci,* 12**,** 1453-65.

FUJITA, I., TANAKA, K., ITO, M. & CHENG, K. 1992. Columns for visual features of objects in monkey inferotemporal cortex. *Nature,* 360**,** 343-6.

GEORGIEVA, S. S., TODD, J. T., PEETERS, R. & ORBAN, G. A. 2008. The extraction of 3D shape from texture and shading in the human brain. *Cereb Cortex,* 18**,** 2416-38.

GOENSE, J. B. & LOGOTHETIS, N. K. 2008. Neurophysiology of the BOLD fMRI signal in awake monkeys. *Curr Biol,* 18**,** 631-40.

GONCALVES, N. R., BAN, H., SANCHEZ-PANCHUELO, R. M., FRANCIS, S. T., SCHLUPPECK, D. & WELCHMAN, A. E. 2015. 7 tesla FMRI reveals systematic functional organization for binocular disparity in dorsal visual cortex. *J Neurosci,* 35**,** 3056-72.

GOODALE, M. A., MILNER, A. D., JAKOBSON, L. S. & CAREY, D. P. 1991. A neurological dissociation between perceiving objects and grasping them. *Nature,* 349, 154-6.

GRILL-SPECTOR, K. & MALACH, R. 2001. fMR-adaptation: a tool for studying the functional properties of human cortical neurons. *Acta Psychol (Amst),* 107**,** 293-321.

GROSS, C. G. 1994. How inferior temporal cortex became a visual area. *Cereb Cortex,* 4**,** 455-69.

HIKOSAKA, K. 1999. Tolerances of responses to visual patterns in neurons of the posterior inferotemporal cortex in the macaque against changing stimulus size and orientation, and deleting patterns. *Behav Brain Res,* 100**,** 67-76.

JAMES, T. W., CULHAM, J., HUMPHREY, G. K., MILNER, A. D. & GOODALE, M. A. 2003. Ventral occipital lesions impair object recognition but not object-directed grasping: an fMRI study. *Brain,* 126**,** 2463-75.

JANSSEN, P., VOGELS, R., LIU, Y. & ORBAN, G. A. 2001. Macaque inferior temporal neurons are selective for three-dimensional boundaries and surfaces. *J Neurosci,* 21, 9419-29.

JANSSEN, P., VOGELS, R., LIU, Y. & ORBAN, G. A. 2003. At least at the level of inferior temporal cortex, the stereo correspondence problem is solved. *Neuron,* 37**,** 693-701.

JANSSEN, P., VOGELS, R. & ORBAN, G. A. 1999. Macaque inferior temporal neurons are selective for disparity-defined three-dimensional shapes. *Proc Natl Acad Sci U S A,* 96**,** 8217-22.

JANSSEN, P., VOGELS, R. & ORBAN, G. A. 2000a. Selectivity for 3D shape that reveals distinct areas within macaque inferior temporal cortex. *Science,* 288**,** 2054-6.

JANSSEN, P., VOGELS, R. & ORBAN, G. A. 2000b. Three-dimensional shape coding in inferior temporal cortex. *Neuron,* 27**,** 385-97.

JOLY, O., VANDUFFEL, W. & ORBAN, G. A. 2009. The monkey ventral premotor cortex processes 3D shape from disparity. *Neuroimage,* 47**,** 262-72.

KAJIKAWA, Y. & SCHROEDER, C. E. 2011. How local is the local field potential? *Neuron,* 72**,** 847-58.

KATZNER, S., NAUHAUS, I., BENUCCI, A., BONIN, V., RINGACH, D. L. & CARANDINI, M. 2009. Local origin of field potentials in visual cortex. *Neuron,* 61**,** 35-41.

KOBATAKE, E. & TANAKA, K. 1994. Neuronal selectivities to complex object features in the ventral visual pathway of the macaque cerebral cortex. *J Neurophysiol,* 71**,** 856-67.

KOURTZI, Z., ERB, M., GRODD, W. & BULTHOFF, H. H. 2003. Representation of the perceived 3-D object shape in the human lateral occipital complex. *Cereb Cortex,* 13**,** 911-20.

KOURTZI, Z. & KANWISHER, N. 2000. Cortical regions involved in perceiving object shape. *J Neurosci,* 20**,** 3310-8.

KREIMAN, G., FRIED, I. & KOCH, C. 2002. Single-neuron correlates of subjective vision in the human medial temporal lobe. *Proc Natl Acad Sci U S A,* 99**,** 8378-83.

KREIMAN, G., KOCH, C. & FRIED, I. 2000a. Category-specific visual responses of single neurons in the human medial temporal lobe. *Nat Neurosci,* 3**,** 946-53.

KREIMAN, G., KOCH, C. & FRIED, I. 2000b. Imagery neurons in the human brain. *Nature,* 408**,** 357-61.

LIU, J. & NEWSOME, W. T. 2006. Local field potential in cortical area MT: stimulus tuning and behavioral correlations. *J Neurosci,* 26**,** 7779-90.

LOGOTHETIS, N. K., PAULS, J., AUGATH, M., TRINATH, T. & OELTERMANN, A. 2001. Neurophysiological investigation of the basis of the fMRI signal. *Nature,* 412**,** 150-7.

LOGOTHETIS, N. K. & SHEINBERG, D. L. 1996. Visual object recognition. *Annu Rev Neurosci,* 19**,** 577-621.

MOORE, C. & ENGEL, S. A. 2001. Neural response to perception of volume in the lateral occipital complex. *Neuron,* 29**,** 277-86.

OOSTENVELD, R., FRIES, P., MARIS, E. & SCHOFFELEN, J. M. 2011. FieldTrip: Open source software for advanced analysis of MEG, EEG, and invasive electrophysiological data. *Comput Intell Neurosci,* 2011**,** 156869.

OP DE BEECK, H., WAGEMANS, J. & VOGELS, R. 2001. Inferotemporal neurons represent low-dimensional configurations of parameterized shapes. *Nat Neurosci,* 4**,** 1244-52.

ORBAN, G. A., ZHU, Q. & VANDUFFEL, W. 2014. The transition in the ventral stream from feature to real-world entity representations. *Front Psychol,* 5**,** 695.

PREMEREUR, E., VANDUFFEL, W. & JANSSEN, P. 2012. Local field potential activity associated with temporal expectations in the macaque lateral intraparietal area. *J Cogn Neurosci,* 24**,** 1314-30.

QUIAN QUIROGA, R., KRASKOV, A., KOCH, C. & FRIED, I. 2009. Explicit encoding of multimodal percepts by single neurons in the human brain. *Curr Biol,* 19**,** 1308-13.

QUIROGA, R. Q., REDDY, L., KREIMAN, G., KOCH, C. & FRIED, I. 2005. Invariant visual representation by single neurons in the human brain. *Nature,* 435**,** 1102-1107.

READ, J. C., PHILLIPSON, G. P., SERRANO-PEDRAZA, I., MILNER, A. D. & PARKER, A. J. 2010. Stereoscopic vision in the absence of the lateral occipital cortex. *PLoS One,* 5**,** e12608.

SAWAMURA, H., ORBAN, G. A. & VOGELS, R. 2006. Selectivity of neuronal adaptation does not match response selectivity: a single-cell study of the FMRI adaptation paradigm. *Neuron,* 49**,** 307-18.

SELF, M. W., PETERS, J. C., POSSEL, J. K., REITHLER, J., GOEBEL, R., RIS, P., JEURISSEN, D., REDDY, L., CLAUS, S., BAAYEN, J. C., et al. 2016. The Effects of Context and Attention on Spiking Activity in Human Early Visual Cortex. *PLoS Biol,* 14**,** e1002420.

SIEGEL, M. & KONIG, P. 2003. A functional gamma-band defined by stimulus-dependent synchronization in area 18 of awake behaving cats. *J Neurosci,* 23**,** 4251-60.

SILSON, E. H., MCKEEFRY, D. J., RODGERS, J., GOUWS, A. D., HYMERS, M. & MORLAND, A. B. 2013. Specialized and independent processing of orientation and shape in visual field maps LO1 and LO2. *Nat Neurosci,* 16**,** 267-9.

SINKKONEN, J., TIITINEN, H. & NAATANEN, R. 1995. Gabor filters: an informative way for analysing event-related brain activity. *J Neurosci Methods,* 56**,** 99-104.

TALLON-BAUDRY, C. & BERTRAND, O. 1999. Oscillatory gamma activity in humans and its role in object representation. *Trends Cogn Sci,* 3**,** 151-162.

TALLON-BAUDRY, C., BERTRAND, O., DELPUECH, C. & PERMIER, J. 1997. Oscillatory gamma-band (30-70 Hz) activity induced by a visual search task in humans. *J Neurosci,* 17**,** 722-34.

TANAKA, K. 1996. Inferotemporal cortex and object vision. *Annu Rev Neurosci,* 19**,** 109-39.

TANAKA, K., SAITO, H., FUKADA, Y. & MORIYA, M. 1991. Coding visual images of objects in the inferotemporal cortex of the macaque monkey. *J Neurophysiol,* 66**,** 170-89.

TSUNODA, K., YAMANE, Y., NISHIZAKI, M. & TANIFUJI, M. 2001. Complex objects are represented in macaque inferotemporal cortex by the combination of feature columns. *Nat Neurosci,* 4**,** 832-8.

VAN DROMME, I. C., PREMEREUR, E., VERHOEF, B. E., VANDUFFEL, W. & JANSSEN, P. 2016. Posterior Parietal Cortex Drives Inferotemporal Activations During Three-Dimensional Object Vision. *PLoS Biol,* 14**,** e1002445.

VAN DROMME, I. C., VANDUFFEL, W. & JANSSEN, P. 2015. The relation between functional magnetic resonance imaging activations and single-cell selectivity in the macaque intraparietal sulcus. *Neuroimage,* 113**,** 86-100.

VANDUFFEL, W., ZHU, Q. & ORBAN, G. A. 2014. Monkey cortex through fMRI glasses. *Neuron,* 83**,** 533-50.

VERHOEF, B. E., VOGELS, R. & JANSSEN, P. 2010. Contribution of inferior temporal and posterior parietal activity to three-dimensional shape perception. *Curr Biol,* 20**,** 909-13.

VERHOEF, B. E., VOGELS, R. & JANSSEN, P. 2012. Inferotemporal cortex subserves three-dimensional structure categorization. *Neuron,* 73**,** 171-82.

VOGELS, R. 1999. Effect of image scrambling on inferior temporal cortical responses. *Neuroreport,* 10**,** 1811-6.

WANDELL, B. A., DUMOULIN, S. O. & BREWER, A. A. 2007. Visual field maps in human cortex. *Neuron,* 56**,** 366-83.

WELCHMAN, A. E., DEUBELIUS, A., CONRAD, V., BULTHOFF, H. H. & KOURTZI, Z. 2005. 3D shape perception from combined depth cues in human visual cortex. *Nat Neurosci,* 8**,** 820-7.

720   WESTWOOD, D. A. & GOODALE, M. A. 2011. Converging evidence for diverging pathways:
721   neuropsychology and psychophysics tell the same story. *Vision Res,* 51**,** 804-11.
722   YAMANE, Y., CARLSON, E. T., BOWMAN, K. C., WANG, Z. & CONNOR, C. E. 2008. A neural code for
723   three-dimensional object shape in macaque inferotemporal cortex. *Nat Neurosci,* 11**,** 1352-
724   60.
725   YAMANE, Y., TSUNODA, K., MATSUMOTO, M., PHILLIPS, A. N. & TANIFUJI, M. 2006. Representation of
726   the spatial relationship among object parts by neurons in macaque inferotemporal cortex. *J
727   Neurophysiol,* 96**,** 3147-56.
728   YOSHOR, D., BOSKING, W. H., GHOSE, G. M. & MAUNSELL, J. H. 2007. Receptive fields in human visual
729   cortex mapped with surface electrodes. *Cereb Cortex,* 17**,** 2293-302.

730

731